JAAS

Journal of Analytical Atomic Spectrometry

rsc.li/jaas

ROYAL SOCIETY
OF CHEMISTRY

JAAS

Check for updates

Efficient and robust image registration for two-dimensional micro-X-ray fluorescence measurements†

Felix Bock,[a] Andreas Gruber,[b] Kerstin Leopold [ID] *[b] and Henning Bruhn [ID] *[a]

X-ray fluorescence spectrometry (XRF) is a technique that allows determining non-destructively the composition of elements within a sample. Focussing the excitation X-ray beam to a small spot that is moved in the x–y-direction relative to the sample adds lateral information. Such a two-dimensional micro-X-ray fluorescence (2D μ-XRF) spectrometer for desktop use is commercially available providing a resolution down to approximately 10 μm. With a μ-XRF spectrometer, it is inexpensive to take many scans of the same sample. With super-resolution methods, these can potentially be combined into a higher-resolution image. As a prerequisite, the misalignments of multiple scans (shifts and rotation) in the subpixel range have to be detected. We present a method for image registration of multiple images based on expander graphs that provides adjustable tradeoffs between registration quality and running time. We evaluate the algorithms on artificial and real μ-XRF data and we argue that our findings show that subpixel information is present in real μ-XRF data. This is a necessary condition for the applicability of multi-image super-resolution techniques to μ-XRF data in future work.

1 Introduction

The measurement of the local distribution of chemical elements, *i.e.* element mapping or imaging, is a highly topical research field in analytical chemistry. Many important conclusions can be drawn from the obtained information on chemical–physical and chemical–biological processes taking place at surfaces and interphases of technical materials, in the environment and in biological systems.[1–3] Among the broad variety of analytical techniques available for element mapping, micro-X-ray fluorescence spectrometry (μ-XRF) in a laboratory set-up combines the advantages of non-destructive sample analysis with those of inexpensive routine measurement of large sample series.[4,5] In commercially available 2D μ-XRF instrumentation poly capillary optics focus the X-ray radiation from an X-ray tube to an excitation spot of 5–25 μm in size. Fast scanning of the sample that is placed on an *x*–*y*-stage provides individual spectra for each measurement spot resulting finally in pixelated element images of the sample. The lateral resolution of these element images is mainly defined by the spot size and brilliance of the X-ray beam. In many fields of application, especially in biological and medical research, higher resolution is most desirable. Therefore, efforts to improve the resolution of laboratory μ-XRF set-ups have been made by several research groups in recent years.[5] Approaches

focus on providing higher brilliance of the X-ray spot by using either alternative sources, like a liquid metal jet X-ray source instead of an X-ray tube,[6] and/or by enhanced focussing optics.[7,8] Another approach is allowing pixels with overlapping spots, *i.e.* applying the so-called oversampling technique. Here, images at pixel sizes down to a few μm can be taken though at this level the resulting scans are already blurry and their effective resolution is worse. Yang *et al.*[9] tackled this issue by measuring the X-ray spot more precisely, which in return allows using common image deblurring techniques to improve the effective resolution of images obtained by oversampling.

As taking several scans with a μ-XRF spectrometer is still inexpensive, techniques of multi-image super-resolution appear attractive: multiple low-resolution images of the same object can be combined into a single high-resolution image.[10] The low-resolution images will normally not be perfectly aligned but be shifted and rotated with respect to each other. These misalignments are the source of the subpixel information that is necessary to compute the high-resolution image. In order to make use of this, the image registration problem, the detection of the shifts and rotations between the images, has to be solved at a subpixel scale.

A large variety of image registration algorithms has been proposed.[11–15] Typically, these algorithms are presented only for pairs of images. If there are more than two images, a common workaround is selecting one image as a reference.[12,13] Then, the other images can be shifted onto this reference image.

The quality of the image registration is quite heavily dependent on the quality of the reference image. This may be

[a]Institute of Optimization and Operations Research, Ulm University, Ulm, Germany
[b]Institute of Analytical and Bioanalytical Chemistry, Ulm University, Ulm, Germany
† Electronic supplementary information (ESI) available. See DOI: https://doi.org/10.1039/d2ja00347c

This journal is © The Royal Society of Chemistry 2023

J. Anal. At. Spectrom., 2023, **38**, 1021–1031 | **1021**

noisy or suffer from artefacts as the image resolution in a super-resolution context is usually at the limit of the imaging device. To reduce the dependency on a single reference image, it has been proposed to determine all shifts simultaneously by minimising a global cost function.[16–18] While this noticeably improves the quality of the registration, it comes with a significant computational burden. We present a method based on expander graphs that provides a trade-off between image registration quality and computation time. We demonstrate its advantages by comparing our method with the single reference method on μ-XRF data.

Besides photo images the image registration problem has already been considered for several medical diagnosis techniques such as mass spectrometry imaging (MSI),[19] computed tomography (CT),[20] and the combination of CT images and ultrasound images.[21] Each type of image comes along with its own challenges.

This article is organised as follows: in Section 2, the parameters of the experiments are stated. In Section 3.1, the registration model is described and in Section 3.2 the algorithms are presented. Finally, in Section 4 the algorithms are evaluated on artificial data and on real μ-XRF measurements.

2 Experimental section

μ-XRF element images are obtained using a Bruker M4 Tornado (software version 1.5.2.48; Bruker Nano GmbH, Berlin, Germany). It is equipped with a rhodium X-ray tube operated at 50 kV and 600 μA. The polychromatic beam is focused via poly capillary lenses to a spot size of approximately 25 μm onto the sample at Mo K_α (17.480 keV). The detector, an XFlash 430, with an active area of 30 mm^2 has a resolution of <145 eV at Mn K_α. To minimise interference with elements in the air, the analyses are carried out at a reduced pressure of 20 mbar. The selected area under investigation in this work is 1000 μm × 500 μm and comprises 250 × 125 pixels resulting in a nominal pixel size of 4 μm × 4 μm. The dwell time is set to 10 ms per pixel. An overall scan takes 10 min. Potassium (K) and calcium (Ca) in real samples are detected at K $K_{\alpha 1}$ (3.312 keV) and Ca $K_{\alpha 1}$ (3.691 keV). Spectra evaluation is performed using M4 Tornado evaluation software version 1.6.0.286.

Cross sections of a Norway maple tree – *Acer platanoides* – with a thickness of 20 μm (GSL1 microtome, Schenkung Dapples, Zürich, Switzerland) are prepared to serve as a real sample. The dried microtome sections are fixed on a silicon wafer (Microchemicals GmbH, Ulm, Germany) in a class-100 laminar flow box (SuSi Super Silent, Spectec GmbH, Erding, Germany) in order to avoid any contamination. Sample carriers are then clamped to a house-made holder attached to the sample stage of the instrument.

3 Theoretical section

3.1 Registration model

In our method, we take several μ-XRF scans of the same sample. We model this mathematically: the data consist of n low-resolution images $I_1, I_2, \ldots, I_n$ (the scans) that arise from an unknown high-resolution image H (the sample) by a process that subjects the high-resolution image to the following transformations in this order:

● T_i: first, an affine transformation that captures the rotation and translation of the ith image (*i.e.*, in between measurements, the sample shifts or rotates a little bit);

● B: blurring due to the measurement optics;

● D: downsampling (*i.e.*, the high-resolution image of the sample is transformed to the low resolution that is supported by the measurement device); and

● N_i: finally, addition of noise.

While T_i and N_i depend on the individual low-resolution image, B and D are the same for every image. In μ-XRF it turns out that the samples do not rotate in between measurements, so that the transformation T_i reduces to a translation by a 2-dimensional shift vector $s_i = (s_{i1}, s_{i2})$, where s_{i1} expresses the shift in the x-direction, and s_{i2} the shift in the y-direction. We will write T_{s_i} for the translation with the shift vector s_i. (We note that, while we concentrate on translations, the presented methods can be generalised to allow rotations as well.)

Ultimately, an estimate of the high-resolution image H is desired. This requires an inversion of the transformations N_i, D, B and T_i. The inversion of the blurring and downsampling operators B and D are hard computational problems that, however, become easier if the translations T_{s_i} are already known. We therefore concentrate here on image registration, the problem of recovering the shift vectors s_i.

We may assume that the images are centered at the origin 0, *i.e.*, that the sum of all shifts cancels out:

$$\sum_{i=1}^{n} s_i = 0 \tag{1}$$

The translation T_{s_i} commutes with B and also with D up to small errors due to interpolation. The shift vectors can thus be recovered by shifting the low-resolution images to the best possible fit.

A method often seen is as follows: pick a reference image I_r and then, for every other image, search for the shift that minimises the sum of squared differences to the reference image:[12,13,22,23]

$$\min_{s_i} \|I_r - T_{s_i}(I_i)\|^2 \tag{2}$$

for every $i \neq r$. Here, $(a, b) = \sqrt{a^2 + b^2}$ denotes the usual Euclidean norm in the plane.

An alternative to the reference image method is to consider all pairs at once by using the sum of all sums of squared differences:

$$\min_{s_1, \ldots, s_n} \sum_{i,j \in \{1, \ldots, n\}} \|I_i - T_{s_i - s_j}(I_j)\|^2 \tag{3}$$

Note that this objective function is symmetric in the sense that all images are treated the same.

There is some fine print. The shifted images have to be evaluated at fractional pixel positions, which requires

interpolation. In this article, we use one of the simplest interpolation methods, bilinear interpolation. Pixels at the border pose another problem. Due to the shifts, there are pixels in one image that are beyond the border of the other image. Since the shifts in our application are at most a few pixels, the cleanest way is to disregard pixels close to the border in the loss function.

3.2 Registration algorithms

Algorithms for image registration have two major competing goals: high accuracy and low running time. In this section, four algorithms are discussed with a different balance of these goals.

The most straightforward way of minimising eqn (3) is to apply a standard solver, such as Nelder–Mead.[24] Nelder–Mead is particularly suited as it does not require a differentiable objective function. Indeed, with bilinear interpolation, the optimisation goal eqn (3) is not differentiable. Instead of Nelder–Mead any other standard algorithm could be used. This would not (much) impact the following discussion. For easier comparability, direct registration (Algorithm 1, Table 1) centers the resulting shifts (line 3).

Minimising eqn (3) is a $2n$-dimensional problem, *i.e.*, the solution is a vector of $2n$ numbers (two for each of the n shifts). As a consequence, the running time will often be large.

Next, let us consider the reference image method eqn (2). If s_i is the true position during measurement i then the pairwise shift $s_{i,r}$ of an image I_i to the reference image I_r satisfies the equation

$$s_{i,r} = s_r - s_i.$$

Thus, the pairwise shifts can be used to compute estimates for the shifts as shown in reference registration (Algorithm 2, Table 2).

The choice of $\hat{s}_r$ in line 2 ensures that the positions are centered as

$$\sum_{i=1}^{n} \hat{s}_i = \hat{s}_r + \sum_{i \neq r} (\hat{s}_r - \hat{s}_{i,r}) = n\hat{s}_r - \sum_{i \neq r} \hat{s}_{i,r} = 0$$

We employ Nelder–Mead in line 1. While direct registration is a single $2n$-dimensional minimisation problem, reference registration makes do with $n - 1$ 2-dimensional minimisation problems. Reference registration is much faster as Nelder–Mead scales super-linearly with the dimension. Accuracy, in

Table 1 Algorithm 1 Direct registration

Input: images $I_1, \ldots, I_n$
Output: estimates for positions $\hat{s}_1, \hat{s}_2, \ldots, \hat{s}_n$
1: Compute a minimum $\hat{s}_1, \ldots, \hat{s}_n$ of eqn (3) with Nelder–Mead
2: Set $c = \dfrac{1}{n} \sum_{k=1}^{n} \hat{s}_k$
3: Set $\hat{s}_k = \hat{s}_k - c$ for every k
4: Return $\hat{s}_1, \hat{s}_2, \ldots, \hat{s}_n$

Table 2 Algorithm 2 Reference registration

Input: images $I_1, \ldots, I_n$ and index of the reference image r
Output: estimates for positions $\hat{s}_1, \hat{s}_2, \ldots, \hat{s}_n$
1: Compute $\hat{s}_{i,r}$ by minimising $\|I_r - T_{\hat{s}_{i,r}}(I_i)\|^2$ for every $i \neq r$
2: Set $\hat{s}_r = \dfrac{1}{n} \sum_{i \neq r} \hat{s}_{i,r}$
3: Set $\hat{s}_i = \hat{s}_r - \hat{s}_{i,r}$ for every $i \neq r$
4: Return $\hat{s}_1, \hat{s}_2, \ldots, \hat{s}_n$

contrast, is reduced. Indeed, the algorithm depends heavily on the quality of the reference image: the noise and artefacts in it will have a great impact on computed shifts. In the hypothetical case, for example, that the reference image is pure noise, the resulting shifts will be completely random.

Let us formalise this insight. Noise makes the estimates $\hat{s}_{i,j}$ for the pairwise shifts differ from the true shifts $\hat{s}_{i,j}$ by an error term of $\varepsilon_{i,j} \in \mathbb{R}^2$:

$$\hat{s}_{i,r} = s_{i,r} + \varepsilon_{i,r} = s_r - s_i + \varepsilon_{i,r}$$

We compute for the estimate $\hat{s}_r$ of the shift of the reference image:

$$\hat{s}_r = \frac{1}{n} \sum_{i \neq r} \hat{s}_{i,r} = \frac{1}{n} \sum_{i \neq r} (s_r - s_i + \varepsilon_{i,r})$$

$$= s_r - \frac{1}{n} \sum_{i=1}^{n} s_i + \frac{1}{n} \sum_{i \neq r} \varepsilon_{i,r} = s_r + \frac{1}{n} \sum_{i \neq r} \varepsilon_{i,r}$$

and for $j \neq r$:

$$\hat{s}_j = \hat{s}_r - \hat{s}_{j,r}$$

$$= \left(s_r + \frac{1}{n} \sum_{i \neq r} \varepsilon_{i,r} \right) - (s_r - s_i + \varepsilon_{i,r})$$

$$= s_j - \frac{n-1}{n} \varepsilon_{j,r} + \frac{1}{n} \sum_{i \notin \{r,j\}} \varepsilon_{i,r}$$

We estimate the variance of the computed $\hat{s}_i$. The estimated shifts $\hat{s}_i$ are 2-dimensional vectors and thus to compute the variance we need to treat each entry (in x- and in y-directions) separately. However, the computation is the same. As we do not want to encumber the notation with another subindex to distinguish between x- and y-entries, we write $\mathrm{Var}[\hat{s}_i]$ to denote the vector consisting of the variance of each entry. For simplicity, we assume that the errors $\varepsilon_{i,j}$ are uncorrelated, and that the variance (of each entry) is bounded by a constant that does not depend on i, j or whether it is the x- or the y-entry. We write ε for the 2-dimensional vector with both entries equal to that constant. We also assume that the mean error is 0, which seems reasonable given the symmetric roles of I_i and I_j.

We use only a basic property of variance: if $X_1, \ldots, X_N$ are uncorrelated random variables, and if $a_1, \ldots, a_N$ and b are constants then $\mathrm{Var}[\sum_{i=1}^{N} a_i X_i + b] = \sum_{i=1}^{N} a_i^2 \mathrm{Var}[X_i]$. We get:

This journal is © The Royal Society of Chemistry 2023

J. Anal. At. Spectrom., 2023, **38**, 1021–1031 | **1023**

$$\mathrm{Var}[\hat{s}_r] = \mathrm{Var}\left[\frac{1}{n}\sum_{i\neq r}\hat{s}_{i,r}\right] = \frac{1}{n^2}\sum_{i\neq r}\mathrm{Var}[\hat{s}_{i,r}] \leq \frac{n-1}{n^2}\varepsilon \leq \frac{1}{n}\varepsilon$$

$$\mathrm{Var}[\hat{s}_j] = \mathrm{Var}\left[s_j - \frac{n-1}{n}\varepsilon_{j,r} + \frac{1}{n}\sum_{i\notin\{r,j\}}\varepsilon_{i,r}\right]$$

$$\leq \frac{n^2-n-1}{n^2}\varepsilon \approx \varepsilon \quad \text{for } j\neq r$$

We see that for an increasing number of scans n, the variance $\mathrm{Var}[\hat{s}_r]$ of the reference image vanishes, while this is not the case for $\hat{s}_i$ with $i \neq r$. Vanishing variance[25] means that, for increasing n, the estimate $\hat{s}_r$ of the reference image is, with high probability, arbitrarily close to the true value s_r. In other words, the more scans are taken, the more likely it is to recover the precise shift. Again, this cannot be guaranteed for other $\hat{s}_i$, i.e., for non-reference images.

In practice, the errors $\varepsilon_{i,r}$ will be correlated. While this may dampen the overall error, it will still be quite noticeable.

To reduce the inaccuracies for non-reference images, pairwise registration (Algorithm 3, Table 3) computes estimates $\hat{s}_{i,j}$ for every pair of images I_i, I_j. Using that the center is 0, i.e. $\sum_{i=1}^{n} s_i = 0$, estimates for the positions are given by:

$$\hat{s}_j = \frac{1}{n}\sum_{i\neq j}\hat{s}_{i,j} = \frac{1}{n}\sum_{i\neq j}(s_j - s_i + \varepsilon_{i,j}) = s_j + \frac{1}{n}\sum_{i\neq j}\varepsilon_{i,j}.$$

This can be interpreted as treating each image as the reference image for its own position. With the same assumptions as above, we obtain

$$\mathrm{Var}[\hat{s}_j] \leq \frac{1}{n}\varepsilon \quad \text{for every } j.$$

In contrast to reference registration, here, the variance vanishes for all images, and thus, for an increasing number of scans, the estimation $\hat{s}_j$ will be, with high probability, arbitrarily close to the true value s_j.

Note that as a side effect of interpolation at a subpixel level, it may make a difference whether the image I_i is compared to I_j, or I_j to I_i. That is

$$\min_{S_{j,i}}\|I_i - T_{\hat{S}_{j,i}}(I_j)\|^2 \neq \min_{S_{i,j}}\|I_j - T_{\hat{S}_{i,j}}(I_i)\|^2.$$

As a consequence, the minimiser $\hat{s}_{i,j}$ of the left-hand side does not need to coincide with the negative of the minimiser of the right-hand side. In practice, however, the difference turns out to be negligible even at a subpixel scale, which is the justification for line 3.

This choice saves on computation time and additionally ensures that the positions are centered:

$$\sum_{j=1}^{n}\hat{s}_j = \frac{1}{n}\sum_{j=1}^{n}\sum_{i\neq j}\hat{s}_{i,j} = \frac{1}{n}\sum_{j=1}^{n}\sum_{i>j}(\hat{s}_{i,j}+\hat{s}_{j,i}) = 0$$

The running time of pairwise registration is mostly determined by the number of pairwise shifts that are computed in line 2. As there are $\frac{n(n-1)}{2}$ pairs $i < j$, the running time grows quadratically in n which results in large running times even for a moderate number n of scans.

It would be desirable to construct an algorithm that uses an intermediate number of pairwise shifts to obtain results that are more precise than reference registration but not as time-consuming as pairwise registration.

This poses the question which pairwise shifts should be computed and how to use them to improve the accuracy.

Which pairwise shifts are computed in the two algorithms is illustrated in Fig. 1. We phrase these observations in the language of graphs.[26] Each image is a vertex of this graph (the numbered circles in the figure), and whenever we directly compute the shift between two images then they are linked by an edge. Thus, for reference registration (Fig. 1a), every image is linked by an edge to the reference image (with index 1 in the figure) but there is no edge between any two non-reference images. The graph is very sparse, i.e. has few edges, which is indicative of a small running time. In contrast, the graph for pairwise registration (Fig. 1b) is very dense as every pair of images is compared, i.e. linked by an edge, resulting in a large running time. The asymmetry of the reference registration graph reflects the poor error asymptotics.

The aim now is to base image registration on a graph (Algorithm 4, Table 4) that is a compromise between the reference registration graph and the pairwise registration graph: sparse but very symmetric, a bit like the graph on the right in Fig. 1. We will discuss below how we choose the graph.

Given a graph for image registration, how do we compute the estimates $\hat{s}_{i,j}$? Whenever two vertices i, j are linked by an edge in such a graph, we directly compute $\hat{s}_{i,j}$. If they are not, then we proceed as in the reference image method: we take a sequence of distinct images $I_i = I_{r_1}, I_{r_2}, \dots I_{r_\ell} = I_j$ such that each of the two consecutive images is linked by an edge, and then compute the shift estimate $\hat{s}_{i,j}$ as the sum of the directly computed shifts. For example, there is no edge between vertices 1 and 3 in the graph of Fig. 1c. But there is an edge from 1 to 2 and from 2 to 3, resulting in the estimate $\hat{s}_{1,3} = \hat{s}_{1,2} + \hat{s}_{2,3}$.

Table 3 Algorithm 3 Pairwise registration

Input: images $I_1, \dots, I_n$
Output: estimates for positions $\hat{s}_1, \hat{s}_2, \dots, \hat{s}_n$
1: For every pair i, j with $i < j$ do
2:    Compute $\hat{s}_{i,j}$ by minimising $\|I_j - T_{\hat{s}_{i,j}}(I_i)\|^2$
3:    Set $\hat{s}_{j,i} = -\hat{s}_{i,j}$
4: End for
5: $\hat{s}_j = \frac{1}{n}\sum_{i\neq j}\hat{s}_{i,j}$ for every j
6: Return $\hat{s}_1, \hat{s}_2, \dots, \hat{s}_n$

1024 | J. Anal. At. Spectrom., 2023, 38, 1021–1031

This journal is © The Royal Society of Chemistry 2023

Fig. 1 Graph representing pairwise shifts that are computed.

In the terminology of graph theory, such a sequence of distinct vertices, with each consecutive pair linked by an edge, is called a path. To reduce the error of the estimates $\hat{s}_{i,j}$, the path $P_{i,j}$ from i to j should have few edges, and we will compute these to have the shortest number of edges possible.

The paths in line 6 can be computed easily with a standard algorithm, breadth-first search.[27] Note that graph registration reduces to reference registration, or to pairwise registration, if the graph is chosen as the one on the left in Fig. 1 or as the one in the middle. The estimates $\hat{s}_{i,j}$ decompose into:

$$\hat{s}_{i,j} = \sum_{r=1}^{\ell} \hat{s}_{i_{r-1},i_r} = s_j - s_i + \sum_{r=1}^{\ell} \varepsilon_{i_{r-1},i_r}$$

This results in errors for the positions as follows:

$$\hat{s}_j = \frac{1}{n}\sum_{i \neq j} \hat{s}_{i,j} = s_j + \frac{1}{n}\sum_{i \neq j}\sum_{r=1}^{\ell} \varepsilon_{i_{r-1}i_r}.$$

To obtain small variances for $\hat{s}_j$ the individual errors $\varepsilon_{r,t}$ should only contribute to a few shortest paths $P_{i,j}$. This can be achieved by choosing a Moore graph[28] as graph G. A Moore graph is highly symmetric. In particular, there is an integer d such that every vertex is linked to precisely d other vertices by an edge. We argue in the appendix (see ESI†) that the variance

$\mathrm{Var}[\hat{s}_{i,j}]$ vanishes with increasing d which implies that, with high probability, $\hat{s}_{i,j}$ converges to $s_{i,j}$ with increasing d. The parameter d, on the other hand, also determines how many edges the graph contains, namely $\frac{1}{2}dn$. As the running time of graph registration depends mainly on the number of edges, we can use the parameter d to fine-tune the balance between precision and running time.

There are, unfortunately, only a few (non-trivial) Moore graphs. It turns out, however, that a random graph is highly likely to share many properties of a Moore graph. A random graph is one where, for a fixed number of vertices, we decide for each potential edge with probability p whether the edge is present or not. There are more sophisticated but not overly complex methods to choose a random graph such that each vertex is incident with precisely d edges.[29]

A key property of Moore graphs is a mathematical property called expansion.[30] We generate a large number (in the hundreds) of random graphs and then test for good expansion. This can be done by inspecting the eigenvalues of the adjacency matrix.[31] Generating many random graphs and then testing for good expansion can be performed very efficiently so that even for hundreds of such graphs, the procedure takes less than a second. Moreover, suitable graphs for typical pairs of n and d could be precomputed and stored in a database, so that the graph is only computed once.

The code for all methods is available on GitHub.[32]

4 Results and discussion

4.1 Data acquisition and pre-processing

We test the algorithms on artificial data and on real micro X-ray fluorescence (μ-XRF) data. For the artificial data, we take a high-resolution image and degrade it as described by the model in Section 3.1. The shifts are drawn independently from a 2-dimensional Gaussian distribution with mean $\mu = 0$ and variance 16 in x- and in y-direction. After drawing all shifts, the shifts are centered at 0. Then the images are blurred with a Gaussian kernel of size 120×120 with standard deviations of 20 in the x-axis and 28 in the y-axis. From each side, 80 pixels are cut off to avoid artefacts at the border. Finally, the images are downsampled with a factor of 4 in both axes and Gaussian noise

---

Table 4 **Algorithm 4** Graph registration

Input: images $I_1, \ldots, I_n$ and suitable graph G
Output: estimates for positions $\hat{s}_1, \hat{s}_2, \ldots, \hat{s}_n$
1: **For** every edge i, j in G **do**
2:     Compute $\hat{s}_{i,j}$ by minimising $\|I_j - T_{\hat{s}_{i,j}}(I_i)\|^2$
3:        Set $\hat{s}_{j,i} = -\hat{s}_{i,j}$
4: **End for**
5: **For** every pair i, j that is not an edge of G **do**
6:     Compute path $P_{i,j} = i_0, i_1, \ldots, i_\ell$ from i to j with min. number of edges
7:     Set $\hat{s}_{i,j} = \sum_{r=1}^{\ell} \hat{s}_{i_{r-1}, i_r}$
8: **End for**
9: Set $\hat{s}_j = \frac{1}{n}\sum_{i \neq j} \hat{s}_{i,j}$ for every j
10: Return $\hat{s}_1, \hat{s}_2, \ldots, \hat{s}_n$

(a) original image

(b) shifted, blurred, and down-sampled low-resolution image with noise

Fig. 2 Artificial data with (a) showing the original image and (b) depicting a sample of a generated low-resolution and blurred image.

is added with mean 0 and a standard deviation of 10. Whenever this results in negative pixel values, the pixel value is set to 0. An example image is shown in Fig. 2.

For the real μ-XRF images, cross sections of a twig of a Norway maple tree – *Acer platanoides* – are prepared and scans are taken with a nominal pixel size of 4 μm × 4 μm. Further experimental details are given in Section 2. The measurements are rather noisy as shown in Fig. 3 for the exemplary element maps of potassium (K) and calcium (Ca).

Typically, noise is assumed to be additive Gaussian noise. In μ-XRF images, however, noise appears to have more a complex behaviour. We found that preprocessing the measurements by blurring with a Gaussian kernel improves the quality of the image registration step. In our experiments, we used a Gaussian kernel of size 7 × 7 with standard deviations of 5 pixels in the x-

and in the y-direction. The image registration results obtained with this pre-processing are described in Section 4.3.

4.2 Measures for evaluation

We compare the algorithms of Section 3.2 on the described artificial and real data. For the artificial data, we measure the
- mean squared error to the (rescaled) ground truth (mse).

The ground truth has to be rescaled according to the factor of the downsampling. Real data make the evaluation much more challenging as there is no ground truth available. We evaluate the algorithms on three measures:
- fit quality (fit).
- path length (path).
- shift differences between the elements (diff).

(a) Photo

(b) K

(c) Ca

Fig. 3 Images of a cross-section of a twig. The pictures show a photo with the investigated area marked by the red rectangle (a) and μ-XRF scans for the elements potassium (b) and calcium (c).

1026 | *J. Anal. At. Spectrom.*, 2023, **38**, 1021–1031

This journal is © The Royal Society of Chemistry 2023

The fit quality (fit) is the most direct measure: we simply determine the value of the objective function eqn (3) for the shifts found by each of the algorithms. This measure, fit, simply shows how well each algorithm manages to minimise the objective function eqn (3). It is not, however, the best measure of how close to the (unknown) true shifts the recovered shifts are since even the true shifts do not have a perfect fit score due to noise.

With the path length method, a variant of permutation tests,[33] we aim to show that the recovered shifts are not random artifacts of the method. There are two extreme scenarios how the shifts $s_1, \ldots, s_n$ arise that each algorithm produces:

(a) The shifts are random artifacts of the algorithm, perhaps because there are no "true" shifts.

(b) The movement of the sample between measurements is reflected in the data, and the algorithm manages to detect the resulting shifts with reasonable accuracy.

Obviously, the truth will be between these two scenarios. With the measure path, we distinguish whether the truth is better represented by scenario (a) or by (b).

In scenario (a), the shifts $s_1, \ldots, s_n$ are the product of a random process that does not take the order of the shifts into account as the algorithms are invariant under permutation of the shifts (the order $s_1, \ldots, s_n$ is not used in any of the algorithms). As a result, the order $s_1, \ldots, s_n$ is not special, and the path $s_1-s_2-\ldots-s_n$ in the plane is not special either. Therefore, we expect its length

$$\ell = \sum_{i=1}^{n-1} \|s_{i+1} - s_i\|$$

to have a typical value. That is, if we draw uniformly at random permutations of the shifts and compute the resulting path lengths, we do not expect to find that ℓ is contained in the q-quantile with very small q.

What happens if scenario (b) holds? Then, arguably, the shifts are best described by a random walk: between two scans, the sample moves a little, and this movement is added to the previous shift. For simplicity, let us assume that the movements $s_{i,i+1}$ between shifts s_i and s_{i+1} in the random walk are distributed according to a 2-dimensional normal distribution with mean 0 and variance σ^2 in each dimension. In this case the length of each movement $s_{i,i+1}$ is distributed according to a Rayleigh distribution with scale parameter σ.[34] Hence, the expected length of each movement $s_{i,i+1}$ is

$$\sqrt{\frac{\pi}{2}}\sigma.$$

This results in an expected total length of the path $s_1-\ldots-s_n$ of

$$(n-1)\sqrt{\frac{\pi}{2}}\sigma.$$

In contrast to scenario (a), if we subject the positions s_i to a random permutation τ we find that the expected length of the path of the permuted positions is roughly

$$\frac{2\sqrt{2\pi}}{15}\sigma n^{\frac{3}{2}}$$

The computation can be found in the appendix.

We see that the expected length of a permutation path grows with $n^{\frac{3}{2}}$ while the length of the random walk path only grows with n. This now allows us to distinguish between the two scenarios. If scenario (a) reflects the truth then the path length of the original scan order has a small probability to be among the 1% shortest paths, say. If, however, scenario (b) is closer to the truth, we expect the path length to be among the 1% shortest. To test this, we generated 10 000 random permutations, computed the path length, and then determined the q-quantile of the path length of the actual scan order. This q-quantile can be seen in the column path of Tables 5 and 6.

As an illustration, we plot in Fig. 4 (top) an artificial example of scenario (b), the path length of a random walk compared to the path lengths of random permutations. The small arrow in the picture on the right side shows that the path length of the scan order is particularly short. Below, we show the same setting for the shifts of direct registration on twig µ-XRF data. While the path of direct registration appears to be the combination of random movement in conjunction with a possible systematic effect, we argue that they show similar phenomena.

When there is a usable signal in more than one element, we can do image registration for each element separately and compare the resulting shifts. If the algorithms work as intended then the corresponding shifts for the different elements should be close to each other.

Whether there are usable signals for more than one element highly depends on the sample. Sometimes, the signal may be

Table 5 Results on an artificial dataset

Algorithm	Time [s]	fit	path	mse
No shift	—	36 923.2	—	1.89770
Reference registration	170.1	9239.6	0.368	0.00353
Graph registration, $d = 4$	325.4	9213.1	0.358	0.00200
Graph registration, $d = 10$	826.7	9203.5	0.378	0.00138
Graph registration, $d = 20$	1668.4	9203.5	0.388	0.00138
Pairwise registration	4183.3	9198.4	0.387	0.00100
Direct registration	113 720.25	9198.3	0.374	0.00100

Table 6 Results on the µ-XRF dataset

Algorithm	Time [s]	fit	path	diff
No shift	—	1431.7	—	—
Reference registration	112.2	492.0	0.000	0.238
Graph registration, $d = 4$	228.4	483.5	0.000	0.131
Graph registration, $d = 10$	575.9	482.4	0.000	0.103
Graph registration, $d = 20$	1151.7	482.5	0.000	0.111
Pairwise registration	2440.8	481.9	0.000	0.087
Direct registration	116 813.0	481.8	0.000	0.094

This journal is © The Royal Society of Chemistry 2023

J. Anal. At. Spectrom., 2023, **38**, 1021–1031 | **1027**

(a) Random Walk

(b) Result of Direct Registration

Fig. 4 Validation of the result of direct registration on the twig μ-XRF data in(b); artificial data from a random walk in (a). The length of the path in the original ordering is compared to random permutations of the same positions. The third panel shows a histogram of path lengths of random orders. For comparison, the path length of the original scan order is marked with an arrow.

too noisy for every element except one. In the twig data, we found that both potassium and calcium gave reasonable results. Consequently, we computed shifts s_i^K and s_i^{Ca}. We report the mean square difference of the shifts

$$\frac{1}{n} \sum_{i=1}^{n} \left\| s_i^K - s_i^{Ca} \right\|^2$$

in column diff. In Fig. 5 the results of direct registration for potassium and calcium are shown. While they do not perfectly align, a clear correlation can be seen. If available, this is a reasonable stand-in for the mse measure.

4.3 Evaluation results

In addition to the evaluation measures, we tabulate the running times. The algorithms were run on an Intel Xeon Gold 6230 with 2.1 GHz and 12 GB memory. For every measure, averages over 10 runs are taken to obtain more reliable results. As a baseline, we also include a row "No shift" which corresponds to zero shifts for every image.

The results of the artificial data created from the flower image in Fig. 2 are shown in Table 5. As predicted, the running times are increasing. Note that the running time for graph registration includes finding a suitable expander graph. This,

however, amounts to well under a second. The fit value is improving but it never reaches zero. This is due to noise, which causes the ground truth itself to have a fit score of 9198.3. In the mse column, the improvements appear to be more significant
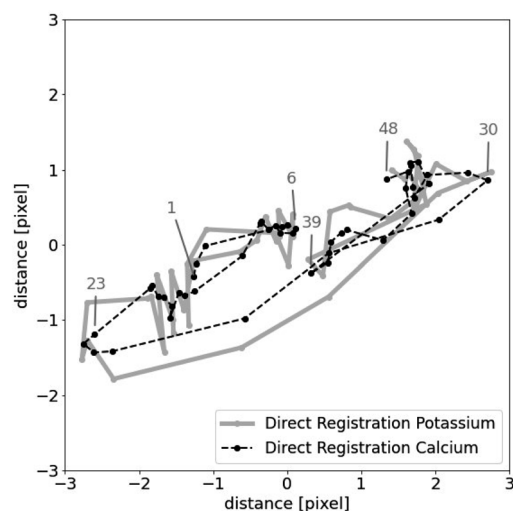

Fig. 5 Results of direct registration of potassium and calcium.

1028 | *J. Anal. At. Spectrom.*, 2023, **38**, 1021–1031

This journal is © The Royal Society of Chemistry 2023

and, indeed, the results get very close to the ground truth. In the column path, all values are about 0.37. That is about 37% of the random permutations result in a shorter path than the original ordering. This is as expected as the artificial shifts were not drawn from a random walk.

We carried out the same experiment for artificial data starting with other high-resolution images. We observed similar results, so we do not report them in detail. The fit values are also leveling off but at different values. This value depends on the size of the image, its brightness, and the noise level. Similarly, the path values are clustered at other values depending on the choice of the random shifts.

Table 6 shows the results for the μ-XRF data. Some representative results can be seen in Fig. 6. It shows similar characteristics as for the artificial data. Column diff appears to work as a reasonable stand-in for mse. A major difference is the column path: the

value is always 0. This strongly indicates that the shifts in the μ-XRF data arise from a random walk. It also shows that every algorithm detects the shift and they only differ in their precision.

The first attempt of using the recovered shifts to compute a single image is shifting the multiple scans on top of each other and using their mean. The resulting higher resolution image of using the shifts of graph registration, with $d = 20$, is shown in Fig. 7. In comparison to the images in Fig. 3, this basic approach already visibly improves the quality of the element map.

The result, however, still looks blurry and there are no sharp edges. This is because the recovered shift is only used to reverse the transformations T_i (see the beginning of Section 3.1) but not the blurring transformation B. Finding the best possible way to reverse this transformation B is part of ongoing research.

(a) REFERENCE REGISTRATION

(b) GRAPH REGISTRATION, degree 10

(c) GRAPH REGISTRATION, degree 20

(d) PAIRWISE REGISTRATION

Fig. 6 Registration results on the twig dataset with the element potassium using (a) reference registration, (b) graph registration with $d = 10$, (c) graph registration with $d = 20$, and (d) pairwise registration. The result of direct registration is shown as a reference in every image.
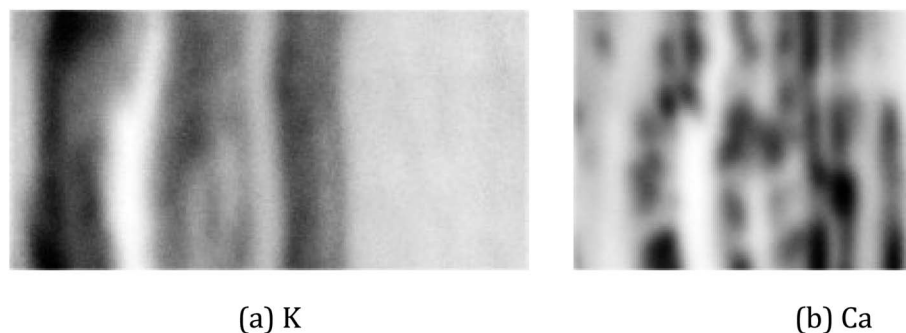
(a) K

(b) Ca

Fig. 7 Shift corrected means of μ-XRF scans (with $n = 48$ scans) of the element potassium (a) and calcium (b); calculated by graph registration, with $d = 20$.

Unfortunately, the quality of the resulting high-resolution image depends on the precision of reversing both transformations T_i and B simultaneously. Therefore, at least visibly, it is hard to see any differences between the shift-corrected means of the different methods proposed in Section 3.2. For a subsequent de-blurring, however, computing the shifts with sufficient precision seems essential.

Finally, computation time might further be decreased by restricting to a smaller area of interest. A first mapping of the complete sample could be followed by repeated scanning of the area of interest, to which then image registration is applied. A certain minimum size of the area of interest is necessary, though, as otherwise boundary effects will deteriorate the recovery quality.

5 Conclusion

We have succeeded for the first time in solving the image registration problem for real μ-XRF data of a biological sample. Our approach provides an adjustable tradeoff between computational time and image registration quality. All tested algorithms are able to recover consistently the shifts in artificial data, and they find shifts in real μ-XRF data that arguably reflect actual processes, the movement of the x–y-stage, during measurement. In particular, the comparison of the shifts with respect to different elements shows that the recovered shifts are reliable on a subpixel scale. Our findings, therefore, confirm the presence of subpixel information in a set of μ-XRF scans. As this is a necessary condition for the application of multi-image super-resolution techniques, our findings constitute a starting point for future improvements in the resolution of laboratory-based μ-XRF analysis. In addition, in future work, the new approach may be tested and adapted to other analytical imaging techniques based on scanning.

Conflicts of interest

There are no conflicts to declare.

Acknowledgements

References

1 C. M. Ackerman, S. Lee and C. J. Chang, Analytical Methods for Imaging Metals in Biology: From Transition Metal Metabolism to Transition Metal Signaling, *Anal. Chem.*, 2017, **89**(1), 22–41.

2 G. Guerriero, I. Stokes, N. Valle, J.-F. Hausman and C. Exley, Visualising Silicon in Plants: Histochemistry, Silica Sculptures and Elemental Imaging, *Cells*, 2020, **9**(4), 1066.

3 D. Hartnell, W. Andrews, N. Smith, H. Jiang, E. McAllum, R. Rajan, F. Colbourne, M. Fitzgerald, V. Lam, R. Takechi and et al, A Review of *Ex vivo* Elemental Mapping Methods to Directly Image Changes in the Homeostasis of Diffusible Ions (Na^+, K^+, Mg^{2+}, Ca^{2+}, Cl^-) Within Brain Tissue, *Front. Neurosci.*, 2020, **13**, 1415.

4 V. K. Singh, N. Sharma and V. K. Singh, Application of x-ray fluorescence spectrometry in plant science: solutions, threats, and opportunities, *X-Ray Spectrom.*, 2022, **51**(3), 304–327.

5 C. Vanhoof, J. R. Bacon, U. E. Fittschen and L. Vincze, Atomic spectrometry update–a review of advances in x-ray fluorescence spectrometry and its special applications, *J. Anal. At. Spectrom.*, 2021, **36**(9), 1797–1812.

6 L. Bauer, M. Lindqvist, F. Förste, U. Lundström, B. Hansson, M. Thiel, S. Bjeoumikhova, D. Grötzsch, W. Malzer, B. Kanngießer and I. Mantouvalou, Confocal micro-x-ray fluorescence spectroscopy with a liquid metal jet source, *J. Anal. At. Spectrom.*, 2018, **33**(9), 1552–1558.

7 L. J. Bauer, R. Gnewkow, F. Förste, D. Grötzsch, S. Bjeoumikhova, B. Kanngießer and I. Mantouvalou, Increasing the sensitivity of micro x-ray fluorescence spectroscopy through an optimized adaptation of polycapillary lenses to a liquid metal jet source, *J. Anal. At. Spectrom.*, 2021, **36**(11), 2519–2527.

8 K. Nakano, A. Matsuda, Y. Nodera and K. Tsuji, Improvement of spatial resolution of μ-XRF by using a thin metal filter, *X-Ray Spectrom.*, 2008, **37**(6), 642–645.

9 J. Yang, Z. Zhang and Q. Cheng, Resolution enhancement in micro-XRF using image restoration techniques, *J. Anal. At. Spectrom.*, 2022, **37**(4), 750–758.

1030 | *J. Anal. At. Spectrom.*, 2023, **38**, 1021–1031

This journal is © The Royal Society of Chemistry 2023

10 L. Yue, H. Shen, J. Li, Q. Yuan, H. Zhang and L. Zhang, Image superresolution: The techniques, applications, and future, *Signal Process.*, 2016, **128**, 389–408.

11 D. I. Barnea and H. F. Silverman, A class of algorithms for fast digital image registration, *IEEE Trans. Comput.*, 1972, **100**(2), 179–186.

12 L. Chen and K.-H. Yap, An effective technique for subpixel image registration under noisy conditions, *IEEE Trans. Syst. Man Cybern. A Syst. Hum.*, 2008, **38**(4), 881–887.

13 M. Guizar-Sicairos, S. T. Thurman and J. R. Fienup, Efficient subpixel image registration algorithms, *Opt. Lett.*, 2008, **33**(2), 156–158.

14 D. Keren, S. Peleg, and R. Brada. Image sequence enhancement using sub-pixel displacements, in *CVPR*, 1988, vol. 88, pp. 5–9.

15 B. D. Lucas and T. Kanade, An iterative image registration technique with an application to stereo vision, *IJCAI*, 1981, pp. 674–679.

16 W. Huizinga, D. H. Poot, J.-M. Guyader, R. Klaassen, B. F. Coolen, M. van Kranenburg, R. Van Geuns, A. Uitterdijk, M. Polfliet, J. Vandemeulebroucke and et al, PCA-based groupwise image registration for quantitative MRI, *Med. Image Anal.*, 2016, **29**, 65–78.

17 C. T. Metz, S. Klein, M. Schaap, T. van Walsum and W. J. Niessen, Nonrigid registration of dynamic medical imaging data using nd+ t b-splines and a groupwise optimization approach, *Med. Image Anal.*, 2011, **15**(2), 238–249.

18 C. Wachinger and N. Navab, Simultaneous registration of multiple images: similarity metrics and efficient optimization, *IEEE Trans. Pattern Anal. Mach. Intell.*, 2012, **35**(5), 1221–1233.

19 B. Balluff, R. M. Heeren and A. M. Race, An overview of image registration for aligning mass spectrometry imaging with clinically relevant imaging modalities, *J. Mass Spectrom. Adv. Clin. Lab*, 2022, **23**, 26–38.

20 H. Dida, F. Charif and A. Benchabane, Image registration of computed tomography of lung infected with COVID-19 using an improved sine cosine algorithm, *Med. Biol. Eng. Comput.*, 2022, 1–15.

21 N. Masoumi, C. J. Belasso, M. O. Ahmad, H. Benali, Y. Xiao and H. Rivaz, Multimodal 3D ultrasound and CT in image-guided spinal surgery: public database and new registration algorithms, *Int. J. Comput. Assisted Radiol. Surg.*, 2021, **16**(4), 555–565.

22 S. Kim and W. Su, Subpixel accuracy image registration by spectrum cancellation, in *1993 IEEE International Conference on Acoustics, Speech, and Signal Processing*, 1993, vol. 5, pp. 153–156.

23 R. Szeliski and et al, Image alignment and stitching: a tutorial, *Found. Trends Comput. Graph. Vis.*, 2007, **2**(1), 1–104.

24 J. A. Nelder and R. Mead, A simplex method for function minimization, *Comput. J.*, 1965, **7**(4), 308–313.

25 Z. Birnbaum, J. Raymond and H. Zuckerman, A Generalization of Tshebyshev's Inequality to Two Dimensions, *Ann. Math. Stat.*, 1947, **18**(1), 70–79.

26 R. Diestel, *Graph Theory*, Springer-Verlag, 5th edn, 2017.

27 T. Cormen, C. Leiserson, R. Rivest and C. Stein, *Introduction to Algorithms*, The MIT Press, 2009.

28 A. J. Hoffman and R. R. Singleton, On Moore graphs with diameters 2 and 3, *IBM J. Res. Dev.*, 1960, **4**(5), 497–504.

29 A. Steger and N. C. Wormald, Generating random regular graphs quickly, *Comb. Probab. Comput.*, 1999, **8**(4), 377–396.

30 M. Dinitz, M. Schapira and G. Shahaf, Approximate Moore graphs are good expanders, *J. Comb. Theory. Ser. B*, 2020, **141**, 240–263.

31 N. Alon, Eigenvalues and expanders, *Combinatorica*, 1986, **6**(2), 83–96.

32 H. Bruhn and F. Bock, *Image Registration Code*, https://github.com/henningbruhn/imgreg, 2023.

33 P. Good, *Permutation Tests: A Practical Guide to Resampling Methods for Testing Hypotheses*, Springer Science & Business Media, 2013.

34 A. Papoulis and S. U. Pillai, *Probability, random variables, and stochastic processes*, Tata McGraw-Hill Education, 2002.

This journal is © The Royal Society of Chemistry 2023

J. Anal. At. Spectrom., 2023, **38**, 1021–1031 | **1031**